Journal of Applied Physics

Magnetic-field-induced incommensurate to collinear spin order transition in $NiBr_2$

Cite as: J. Appl. Phys. **125**, 093902 (2019); https://doi.org/10.1063/1.5066625
Submitted: 16 October 2018 . Accepted: 20 February 2019 . Published Online: 05 March 2019

S. Babu, K. Prokeš, Y. K. Huang, F. Radu, and S. K. Mishra

Journal of Applied Physics ARTICLE scitation.org/journal/jap

Magnetic-field-induced incommensurate to collinear spin order transition in $NiBr_2$

Cite as: J. Appl. Phys. **125**, 093902 (2019); doi: 10.1063/1.5066625
Submitted: 16 October 2018 · Accepted: 20 February 2019 ·
Published Online: 5 March 2019

View Online Export Citation CrossMark

S. Babu,[1] K. Prokeš,[2,a)] Y. K. Huang,[3] F. Radu,[4] and S. K. Mishra[1,b)]

AFFILIATIONS

[1]School of Materials Science and Technology, Indian Institute of Technology, Banaras Hindu University, Varanasi 221005, India
[2]Helmholtz-Zentrum für Materialien und Energie, Hahn-Meitner-Platz 1, Berlin D-14109, Germany
[3]Van der Waals-Zeeman Institute, University of Amsterdam, Science Park 904, Amsterdam, The Netherlands
[4]Helmholtz-Zentrum für Materialien und Energie, Albert-Einstein-Straße 15, Berlin D-12489, Germany

[a)]**Electronic mail:** prokes@helmholtz-berlin.de
[b)]**Electronic mail:** shrawan.mst@iitbhu.ac.in

ABSTRACT

The triangular spin lattice of $NiBr_2$ is a canonical example of the frustrated helimagnet that shows a collinear commensurate antiferromagnetic to an incommensurate spin helix phase transition on cooling. Herein, we have studied a self-flux grown $NiBr_2$ single crystal by neutron diffraction and low temperature magnetization measurements at fields up to 14 T. Experimental findings enable the deduction of the driving force responsible for the spin spiral ordering. The neutron diffraction data reveal satellite peaks representing characteristic features of an incommensurate magnetic state. The satellites develop symmetrically below $T_N = 44.0(1)$ K, replacing the main magnetic reflections. Interestingly, a field-induced incommensurate to commensurate spin phase transition has been successfully demonstrated, which enforces the spin helix to restore the high temperature compensated antiferromagnetic structure. This reorientation can be described by a spin-flop in the (a–b) basal plane of a triangular spin lattice system. The findings offer a novel way for spin helix control of incommensurate phases, having immense scientific and technological implications in the next-generation data storage devices.

I. INTRODUCTION

Noncollinear spins are generic to systems with spin spirals, spin helicoids, canted spins, and magnetic domain walls. Such spin systems have attracted significant interest in recent research activities due to their potential in ultra-dense magnetic storage devices.[1–3] The spin helix usually evolves by breaking the inversion symmetry present and shows several unusual physical phenomena like electric excitation of magnon,[4,5] magnetic skyrmions, and so on[6,7] Among various microscopic driving mechanisms which produce noncollinear spin ordering, Dzyaloshinskii–Moriya interaction (DMI) has found acceptance in many systems.[8,9]

Noncollinear spin arrangements in helimagnets can also result from the presence of competing Heisenberg ferromagnetic and antiferromagnetic (AF) interactions.[10–13] Considering the exchange interaction model in a magnetic field of intensity H, the Hamiltonian **H** for a triangular lattice can be expressed as

$$\mathbf{H} = -J_1\Sigma_{\langle i,j\rangle}S_i \cdot S_j - J_{2,3}\Sigma_{\langle\langle i,j\rangle\rangle}S_i \cdot S_j - H\Sigma_i S_i, \quad (1)$$

where $\Sigma_{\langle i,j\rangle}$ and $\Sigma_{\langle\langle i,j\rangle\rangle}$ represent the sum over the nearest neighbors (*nn*) and the next nearest neighbors (*nnn*), respectively.[10] For a ferromagnetic state ($J_1 > 0$) with *nn* interaction only, the ground state is commensurate with the underlying lattice. On the other hand, for competing interactions ($J_1 > 0$) and the AF third-neighbor interaction ($J_3 < 0$), an incommensurate ground state is more favorable.[10,14–17]

Transition metal dihalides have long been considered as prototypes of antiferromagnets displaying a triangular lattice.[18–24] Most of the previous investigations were focused on the coupling of magnetism and ferroelectricity[19,20] in dihalides. $NiBr_2$, an archetypal dihalide, displays a paramagnetic-to-antiferromagnetic phase transition at

$T_N = 44.0(1)$ K and an antiferromagnetic-to-incommensurate spin spiral at $T_m = 22.8(1)$ K.[22–24] The ground state of the incommensurate spin spiral depicts a threefold degeneracy with respect to the three equivalent wave vectors and is believed to be the source of various distinctive ordered states like the multiple-q state, which otherwise can assume a skyrmionic state, proposed by Okubo *et al.*[25]

In this work, incommensurate helix phase characteristics have been investigated in the single crystal $NiBr_2$ using magnetization (dc and ac), susceptibilities, neutron diffraction, and small-angle neutron scattering. The experimental findings not only indicate an incommensurate spiral ground state known for $NiBr_2$ but also reveal evidence for a magnetic-field-induced spin reorientation, i.e., from the incommensurate spiral to a collinear commensurate phase.

II. METHODS AND EXPERIMENTAL DETAILS

High-quality single crystals of $NiBr_2$ were grown with a self-flux growth method taking a stoichiometric mixture of Ni and Br at the University of Amsterdam as per details reported earlier.[19–21] $NiBr_2$ crystals grew naturally in a layered shape that efficiently cleave along the c-axis. Ni ions occupy a single site in the Bravais lattice as shown in Fig. 1(a). Magnetic measurements were carried out using the MPMS 7 T device and (Quantum Design) PPMS 14 T system, in temperature ranges across 2-300 K at fields up to 14 T applied along and perpendicular to the basal plane.

The diffraction experiments were carried out with neutron diffractometers (E2 and E4) and the small-angle neutron scattering instrument (V4) at the BER II reactor of the Helmholtz-Zentrum Berlin (HZB).[26] E2 and E4 instruments use a pyrolytic graphite (002) monochromator, selecting the neutron wavelength $\lambda = 2.4$ Å. The diffraction data were collected with a two-dimensional, position sensitive ^{3}He detectors. $\frac{\lambda}{2}$ filters were used at both E2 and E4 instruments, which implies a residual higher-order wavelength contamination at a level of less than 10^{-4}. The small-angle neutron scattering measurements were carried out on the V4 instrument that possesses a large position-sensitive detector.

The structure refinements were performed with the Fullprof[27,28] program. During refinements, the nuclear scattering lengths b(Ni) = 1.03 fm and b(Br) = 0.6795 fm were considered. For the absorption correction (Gaussian integration), we used the absorption coefficient $\mu = 0.12\ cm^{-1}$. No secondary extinction corrections were applied.

III. RESULTS AND DISCUSSIONS

A. Magnetization and susceptibility

Figure 2(a) illustrates the temperature dependence of the magnetic susceptibility (χ) of $NiBr_2$, at magnetic fields (H) ranging from 1.0 to 14.0 T, applied perpendicular to the c-axis. At higher temperatures, magnetization is directly proportional to the applied magnetic field such that $\chi(M/H)$ values remain the same for all of magnetic fields.

At lower temperatures, two well-distinguished anomalies are discernible, marking the magnetic phase transitions. For example, at $H = 1$ T, the transition occurs from paramagnetic-to-antiferromagnetic state at $T_N = 44.6(1)$ K. A closer inspection reveals that the transition temperature decreases with an increase in the magnetic field. The second transition from antiferromagnetic to helical spin order state takes place at $T_m = 21.8\,(1)$ K.

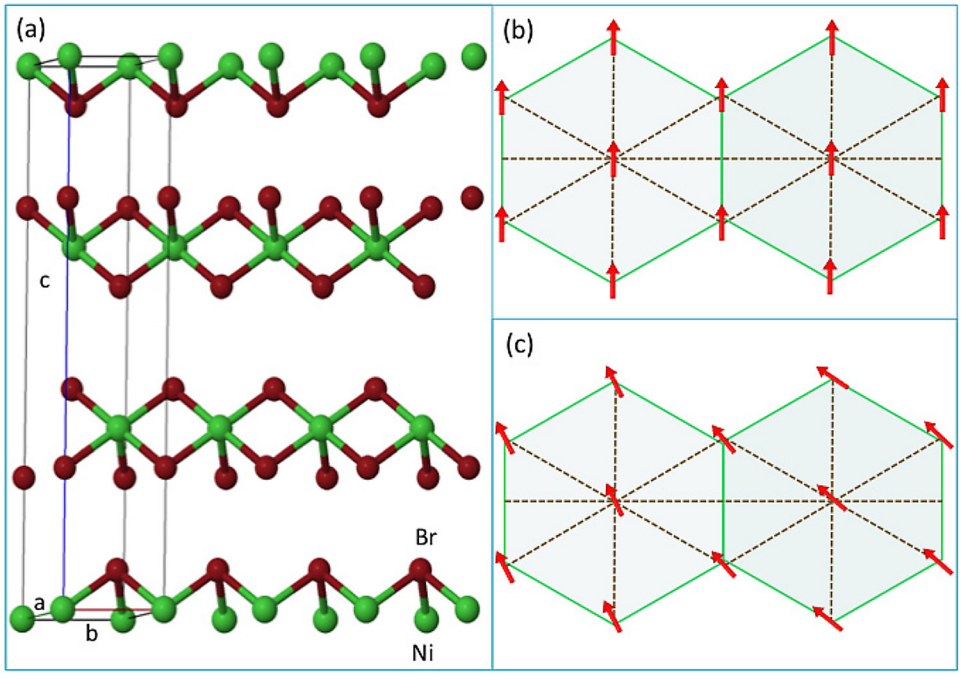

FIG. 1. (a) Schematic representation of the crystal structure of $NiBr_2$. Green and accent small spheres represent Ni and Br ions in a layered triangular lattice, respectively. a, b, and c are the principal axes of the hexagonal cell, where c is the high-symmetry axis. (b) and (c) depict the collinear antiferromagnetic (AF) ($T_m < T < T_N$) and helical spin ($T < T_m$) structures, respectively. Solid arrows indicate spin directions on Ni^{2+} ions. For simplicity, bromide ions are not shown in (b) and (c).

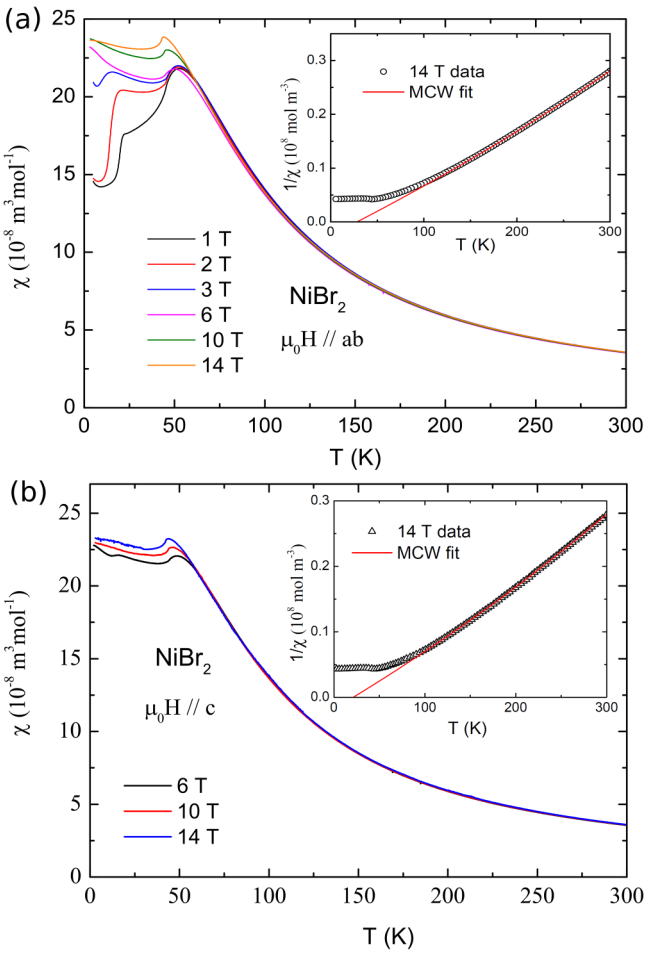

FIG. 2. Temperature dependence of the magnetic susceptibility of $NiBr_2$ measured with field was applied parallel to (a) (*a*–*b*) basal plane and (b) along the *c*-axis, respectively. The insets show the temperature dependence of the inverse magnetic susceptibility $1/\chi(T)$ measured at 14 T in both respective panels. The red solid line is the best fit of $1/\chi(T)$ to a modified Curie–Weiss law.

The $1/\chi$ versus T plot is shown in the inset of Figs. 2(a) and 2(b). It fits with Curie-Weiss law expressed by

$$\chi = C/(T - \theta_p) + \chi_0, \quad (2)$$

where C represents the Curie constant, θ_p is the paramagnetic Curie temperature, and χ_0 denotes the temperature-independent term. The best fit to the Curie-Weiss law is observed above 70 K. Accordingly, data acquired at 1.0 T yield the effective moment $\mu_{eff} = 2.76(1)\mu_B$, which is approximately the same as expected for the Ni ions ($3d^8$, $S = 1$). The effective moment at 14.0 T amounts to $2.66\,(1)\mu_B$. The fitted values of θ_p amount to 22.2(1) K and 28.1 (1) K for the data recorded at 1.0 T and 14.0 T, respectively.

Figure 2(b) shows the temperature dependence of magnetic susceptibility (χ) measured at various fields applied along the *c*-axis. In this orientation, the magnetic susceptibility behavior is similar as described above, at both higher and lower temperatures. The effective magnetic moment and the paramagnetic Curie temperature found are $\mu_{eff} = 2.74(1)\mu_B$ and $\theta_p = 21.3\,(1)$ K, respectively.

The similarity observed in susceptibility at magnetic fields applied along and perpendicular to the *c*-axis above $T > 70$ K indicates negligible anisotropy in the paramagnetic state of $NiBr_2$. However, at temperatures below T_N, χ–H curves for fields applied perpendicular and along the *c*-axis exhibit entirely different magnetization behaviors, as depicted in Figs. 3(a) and 3(b). For the field applied within the (*a*–*b*) basal plane, a clear field-induced transition that shifts to lower fields upon increasing temperature is

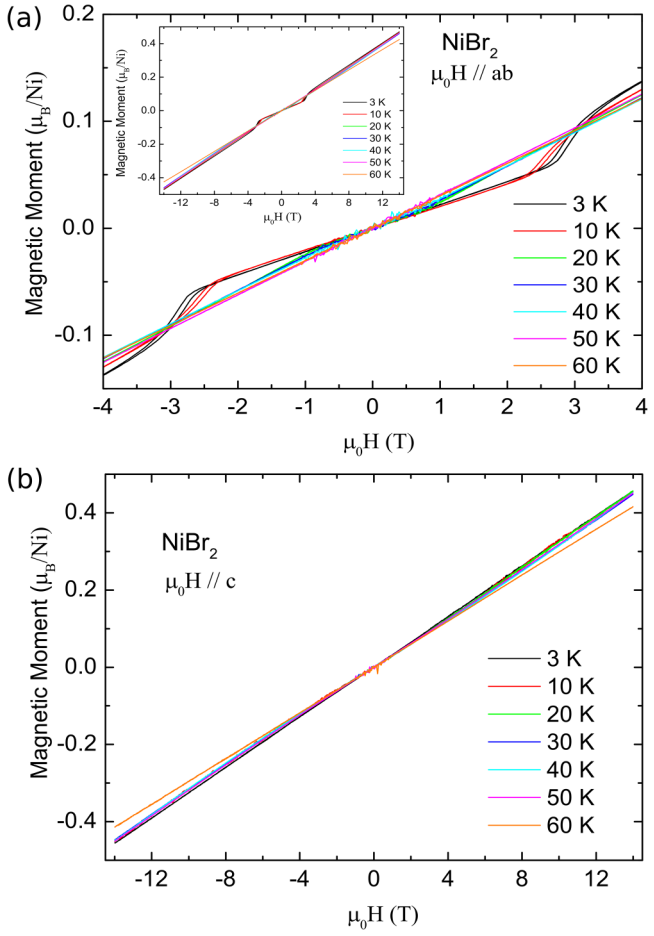

FIG. 3. (a) Field dependence of the $NiBr_2$ magnetization applied perpendicular to the *c*-axis for various temperatures. The full field range ($\pm$14 T) of M–H curves are shown in the inset. (b) Field dependence of the $NiBr_2$ magnetization applied along the *c*-axis measured at various representative temperatures between 3 K and 60 K.

observed. Notice the steps associated with the transition in Fig. 3(a), and the value being $0.036\,\mu_B$/Ni at 3 K.

The phase transitions observed through temperature and magnetic field dependent ac-magnetic susceptibility (χ_{ac}) can now be discussed. χ_{ac} is a complex entity and expressed as $\chi_{ac} = \chi' - i\chi''$. Its real component ($\chi'$) related to the reversible magnetization processes is always in-phase with the oscillating field. The imaginary component (χ'') is associated with losses during irreversible magnetization processes. The ac susceptibility measurements were carried out as a function of temperature at different applied magnetic fields. To minimize the demagnetization effects, the dc magnetic field was applied within the basal plane (a–b). Figure 4(a) illustrates the temperature dependence curves of the ac susceptibility measured in the vicinity of magnetic transitions (below 70 K). The results over the field range of 0.1 to 2.0 T show the maxima near phase transition. Over T_m, at low field strengths, the maxima shift towards a higher temperature.[20]

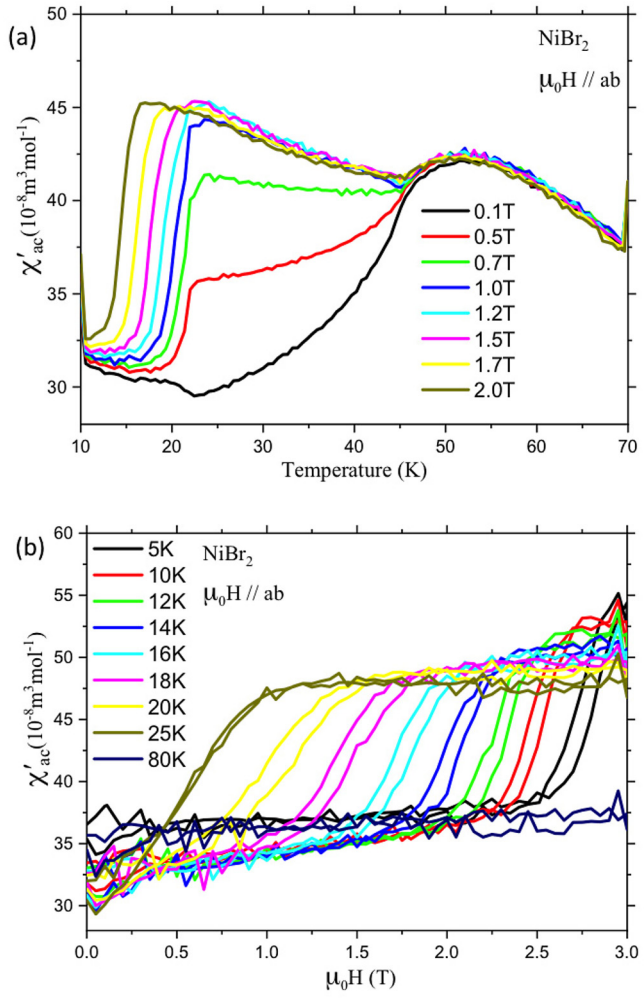

FIG. 4. (a) The temperature dependence of the ac susceptibility, $\chi(H, T)$ of $NiBr_2$ in the vicinity of the lower transition(s), near 50 K, measured in various static applied fields between 0.1 and 2.0 T. Isothermal ac susceptibility $\chi(H, T)$ measured over the range $5\,K \leq T \leq 80\,K$, $0.0 \leq H \leq 3.0\,T$. (b) The hysteresis regime corresponds to the incommensurate phase, $5\,K \leq T \leq 25\,K$. For higher temperature $25\,K \leq T \leq 80\,K$, $\chi(H, T)$ shows a straight line confirming the compensated antiferromagnetic phase area.

Figure 4(b) shows the χ' versus $\mu_0 H$ curves at different temperatures in the range of 5-80 K. At $T = 80$ K, the χ' exhibits a nearly field independent curve. At $T = 25$ K, a peak can be noticed close to the upper phase boundary of the antiferromagnetic state as shown in Fig. 2(a). Below T_m, a hysteretic nature of $\chi'(H, T)$ curves is observed, confirming the signature of the helix nature of noncollinear spins. The shift in peak position with the magnetic field corresponds to the difference in torque required to reverse the helical spins by the applied magnetic field. These results indicate the transition from an incommensurate to a commensurate phase. The peak positions in $\chi'(H, T)$ over the wide ranges map directly onto the field-induced modulation of the incommensurate phase. It should be noted that in the zero field, χ' diminishes monotonically in the temperature range of 5–20 K.

B. Neutron diffraction on $NiBr_2$ crystal

$NiBr_2$ crystallizes in the $CdCl_2$ type rhombohedral structure having lattice constants on hexagonal axes as $a = 3.723$ Å and $c = 18.340$ Å and space group D_{3d}^5 [18–20,22,23] with Ni and Br atoms assuming the Wyckoff positions $3a(0,0,0)$ and $6c(0,0,z)$ with 3 m and -3 m local symmetries, respectively.[22,23] The space group D_{3d}^5 leads to specific extinction conditions $-h + k + l = 3n$ and $-h + k = 3n$ for $hkil$ and $hki0$ reflections, respectively.

Figure 5(a) illustrates the neutron diffraction pattern recorded at 50 K. It displays 110, 003, 006, and 009 Bragg reflections along with the signal originating from the Al-sample holder/cryostat. The refinement shows a reasonable agreement with the literature.[22,23] For $T_m < T < T_N$, additional Bragg reflections associated with the antiferromagnetic order appear and can be indexed with a propagation vector $q_c = (0\ 0\ 3/2)$. As for example, the diffraction pattern recorded at 26 K and presented in Fig. 5(b) contains (0 0 3/2), (0 0 9/2), and (0 0 15/2) magnetic satellites. These corroborate with the antiferromagnetic ordering of Ni spins in the basal plane (a–b).[22,23,26,29] At $T = 50$ K, the signature of a short-range order can also be noticed around q_c [Fig. 5(a)].

A significant change occurs in the diffraction pattern below $T_m = 21.1$ K, as original magnetic reflection (0 0 3/2) [see the inset of Fig. 5(b)] splits and six new Bragg reflections replace each commensurate magnetic reflection. In order to determine the tiny incommensurate components, the neutron beam of longer wavelength ($\lambda = 2.4$ Å) was selected with the pyrolytic graphite monochromator and graphite filters employed to remove the $\lambda/2$ contamination. The signal-to-noise ratio was optimized by varying the slit widths.[26,29] This exercise gives the propagation vector as $q_i = (q_h\ q_h\ 3/2)$ with $q_h \sim 0.03$. The component along the c-axis remains commensurate with $k_z = 3/2$. Thus, the incommensurate component lies along $\langle 110 \rangle$ in the (a–b) plane. Indeed, the q_h varies with temperature in the range 4.2-21.8 K. The absence of higher harmonics [Fig. 5(c)] is indicative of the helical spin order present in the (a–b) plane.

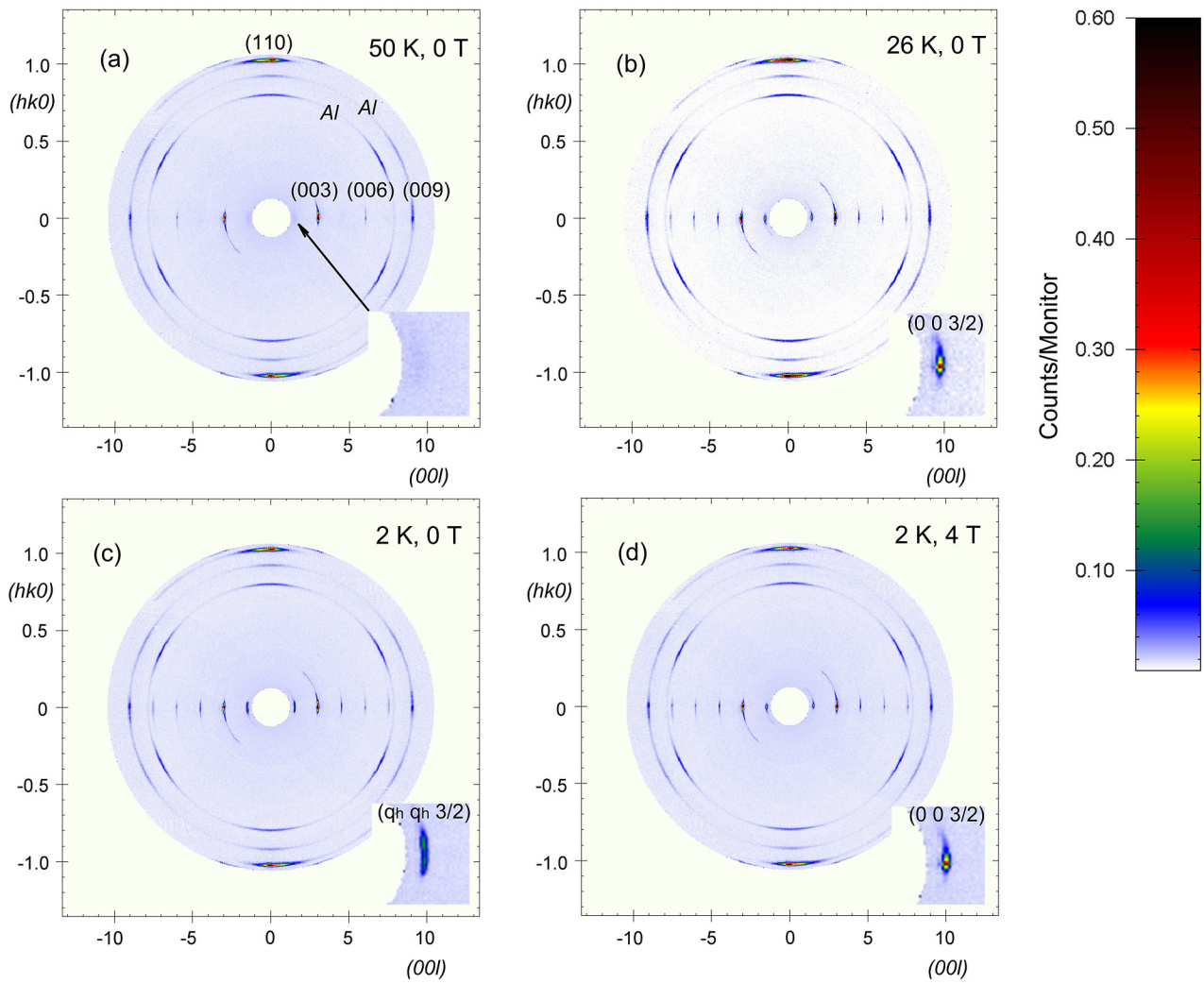

FIG. 5. Diffraction patterns of the $NiBr_2$ single crystal in the (*hhl*) plane at mentioned conditions: (a) 50 K, 0 T, (b) 26 K, 0 T, (c) 2 K, 0 T, and (d) 2 K, 4 T applied within the ($a - b$) basal plane. Insets show the highlighted area around the (0 0 3/2) reciprocal space position.

When an in-plane magnetic field ($H \geq 4$ T) is applied the satellites revert back their shape and position to the commensurate antiferromagnetic phase. Figures 5(c) and 5(d) show the diffraction pattern recorded at 2 K without magnetic field and with 4 T, respectively. This field-induced spin reorientation of incommensurate spins has been examined further within the framework of spin-flop coupling.

Figure 6 shows intensity of the (0 0 3/2) reflection recorded with the zero magnetic field on cooling below 57 K. The solid line (red) represents the best fit of the experimental data satisfying the empirical relation

$$I(T) = b + I_0\left(1 - \frac{T}{T_N}\right)^{2\beta}, \tag{3}$$

where b denotes the background intensity, I_0 represents the intensity at 0 K, and β stands for the critical parameter related to the dimensionality of the system. Above 40 K, the best fit for above empirical relation in the range 40-45 K corresponds to a magnetic phase transition at $T_m = 44.5\,(6)$ K with $\beta = 0.30\,(1)$. However, non-negligible intensity above the background level in Fig. 6 as highlighted by the dashed line (red) above the T_N point confirms the presence of critical scattering in this material. The second transition takes place at T_m. The non-zero intensity below T_m arises due to six new magnetic satellites, emerging in place of the original (0 0 3/2) Bragg reflection.

Figure 7(a) shows the diffraction pattern at 2 K with the zero magnetic field as projected on the $\omega - \nu$ plane, where ω is the sample rotation angle and ν is the deviation angle from the scattering plane.

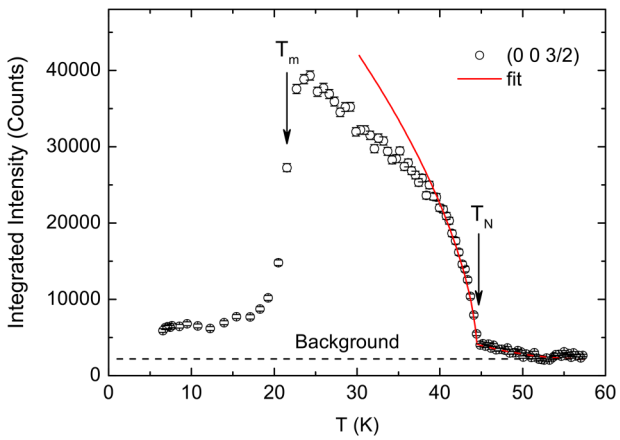

FIG. 6. The temperature dependence of the magnetic (0 0 3/2) Bragg reflection measured upon cooling at the top of the reflection. The solid line through the points just below the T_N is the best fit to Eq. (4) given in the text. The transition at T_m takes place at 21.6 (5) K. Just above the T_N, a magnetic diffraction signal due to short-range correlations is visible. This is highlighted by a dashed line.

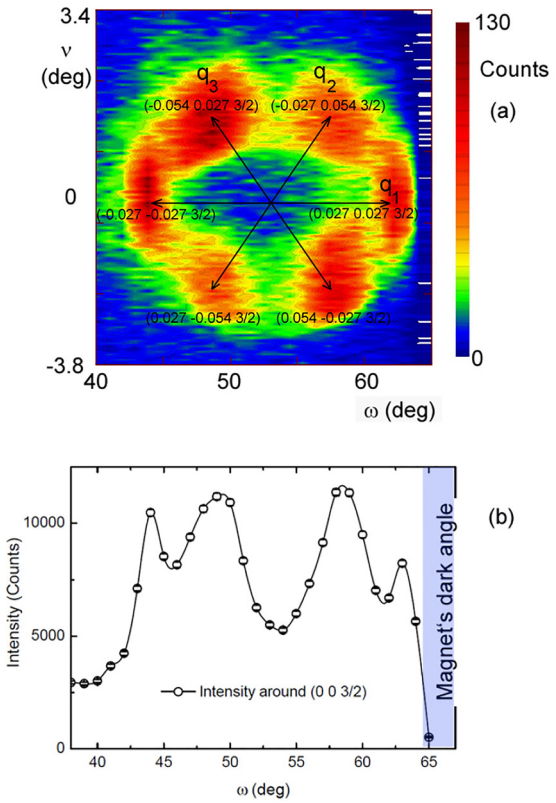

FIG. 7. (a) The diffraction pattern recorded with the zero field around the (0 0 3/2) magnetic reflections in reciprocal space using $\omega-\nu$ projection. (b) The conventional projection of diffraction pattern on the rotational ω-axis.

It is evident that original reflection splits into six reflections corresponding to propagation vectors $\pm q_1 = (q_h\ q_h\ 3/2)$, $\pm q_2 = (-q_h\ 2q_h\ 3/2)$, and $\pm q_3 = (-2q_h\ q_h\ 3/2)$. The UB matrix refinement from nuclear Bragg reflections and positions of the maxima turn out to be $q_h = 0.027\,(1)$, which is in agreement with the literature.[30,31] The six magnetic reflections shown in Fig. 7(a) can be indexed as $(-0.027\ -0.027\ 3/2)$, $(-0.054\ 0.027\ 3/2)$, $(-0.027\ 0.054\ 3/2)$, $(0.027\ 0.027\ 3/2)$, $(0.054\ -0.027\ 3/2)$, and $(0.027\ -0.054\ 3/2)$.

The existence of six magnetic propagation vectors at low temperatures can be explained by two limiting models. In the first case, a homogeneous state where the magnetic moments of Ni are modulated by a uniform propagation vector. In the second, spatially disjoint domains exist, each having its own propagation vector. Since the reflection described by q_3 is about 50% more intense than that of $-q_2$ reflection [see Fig. 7(a)], the first model can be altogether ruled out. Thus, the magnetic structure is essentially described by well separated single-q domains.

Figures 8(a) and 8(b) shows the temperature dependence of the diffracted intensities projected on the ω-axis and $\omega-\nu$ plane, respectively, at various temperatures (2-50 K). It is evident that the incommensurate reflections collapse at T_m into a single (0 0 3/2) reflection.

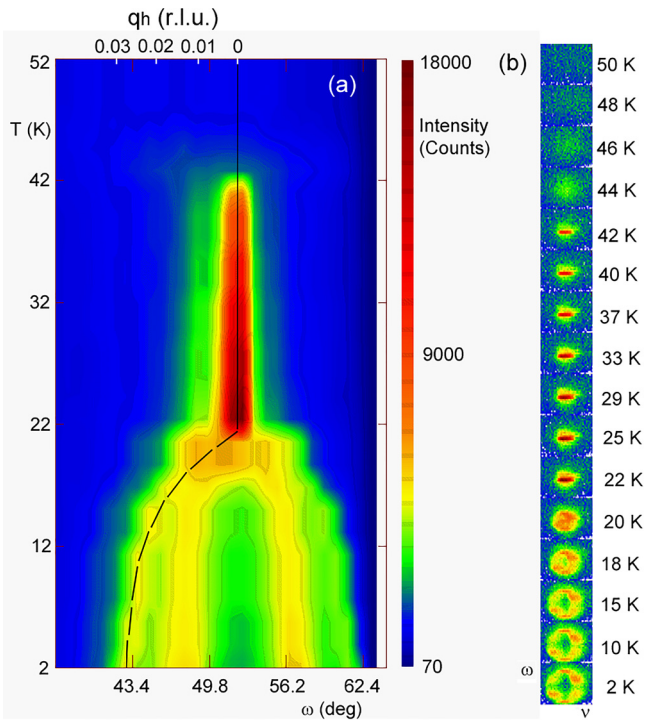

FIG. 8. (a) The temperature dependence of the diffracted signal around the magnetic (0 0 3/2) Bragg reflection projected on the ω-axis. At the top, we show projection of the recorded signal on the reciprocal [110] axis. The incommensurate component q_h is shown by the dashed line. It becomes zero above T_m. (b) Detected signal as seen on the 2D detector on E4 at various temperatures in the zero field.

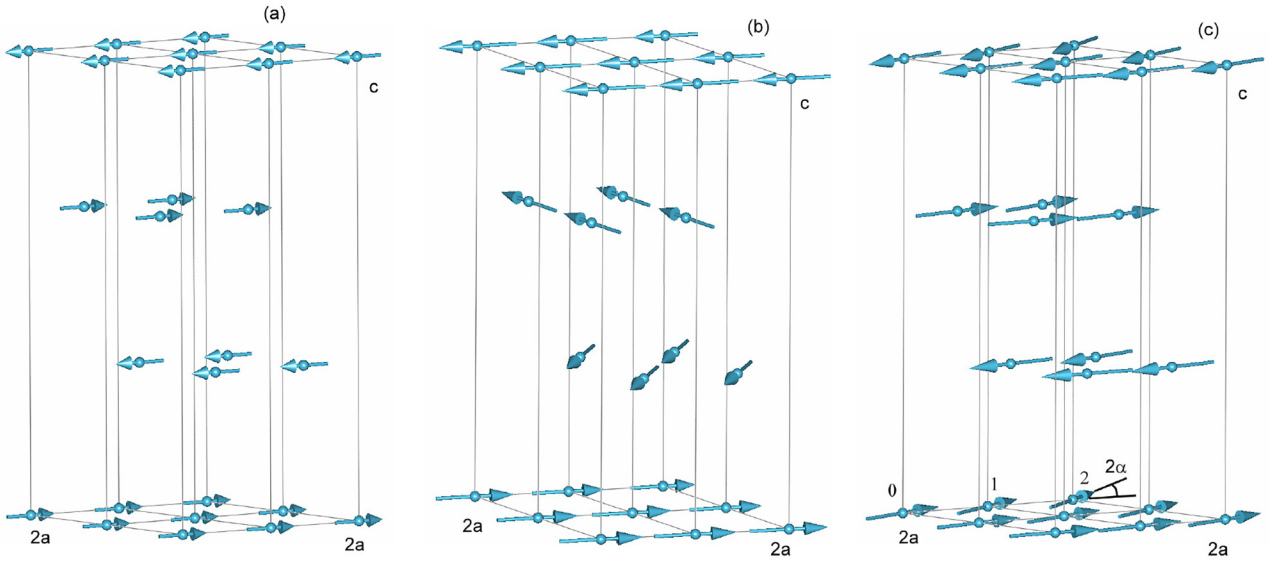

FIG. 9. Schematic representation of $NiBr_2$ structure at 26 K, 0 T (a) and 2 K, 0 T (b). (c) A possible solution that agrees with data taken at 26 K, 0 T equally well. Only Ni atoms are shown. In all cases, $2 \times 2 \times 1$ crystallographic unit cells are shown. The moments in underlying cell along the *c*-axis are reverted.

A dashed line in Fig. 8(a) shows the temperature dependence of the incommensurate component (q_h) of the projection on the q_i vector, originating from (0.027, 0.027, 3/2) reflection and becoming commensurate at T_m, represented by a solid line. Symmetry analysis suggests the direction of the nickel magnetic moment lying either along or perpendicular to the *c*-axis. However, the non-zero intensity of the (0 0 3/2) reflection suggests that moments are oriented within the (*a*–*b*) plane. The best fit of data collected under zero field at 25 K, corresponds to the Ni moment of 2.8 (2) μ_B, which is higher than that reported earlier.[22,23] There are other feasible magnetic structures which agree equally well with the experimental data. Figures 9(a) and 9(b) show two such solutions with collinear alignment of Ni moments. The best fit of data taken at 2 K under the zero field [shown in Fig. 5(c)] using six propagation vectors $q_1 = (-0.027\ -0.027\ 3/2)$, $q_2 = (-0.054\ 0.027\ 3/2)$, $q_3 = (-0.027\ 0.054\ 3/2)$, $q_4 = (0.027\ 0.027\ 3/2)$, $q_5 = (0.054\ -0.027\ 3/2)$, and $q_6 = (0.027\ -0.054\ 3/2)$ gives the Ni magnetic moment 3.0 (3) μ_B. The direction of the Ni moment changes

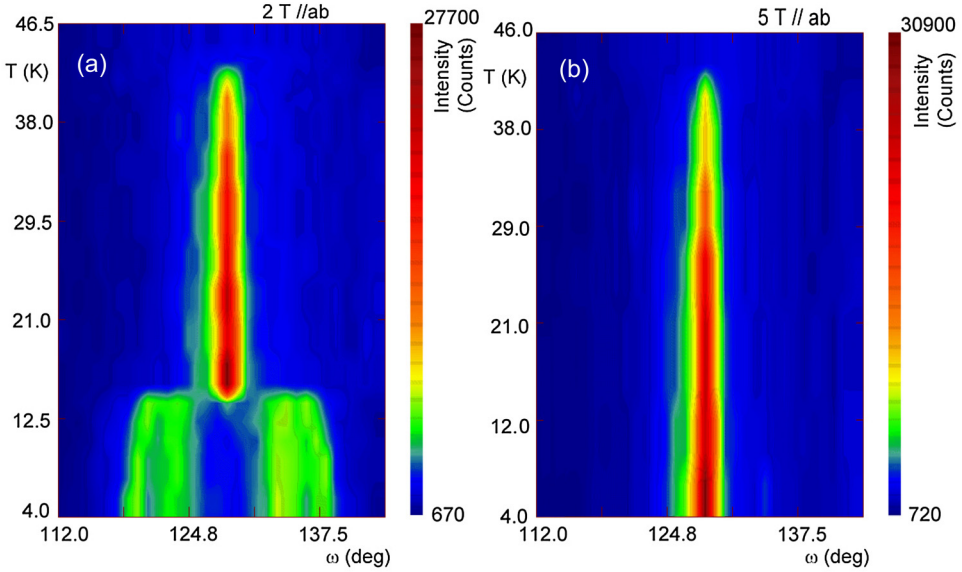

FIG. 10. (a) Temperature dependence of the intensity around the (0 0 3/2) measured with field of 2 T applied within the (*a*–*b*) plane. (b) Temperature dependence of the intensity around the (0 0 3/2) measured with field of 5 T applied within the (*a*–*b*) plane.

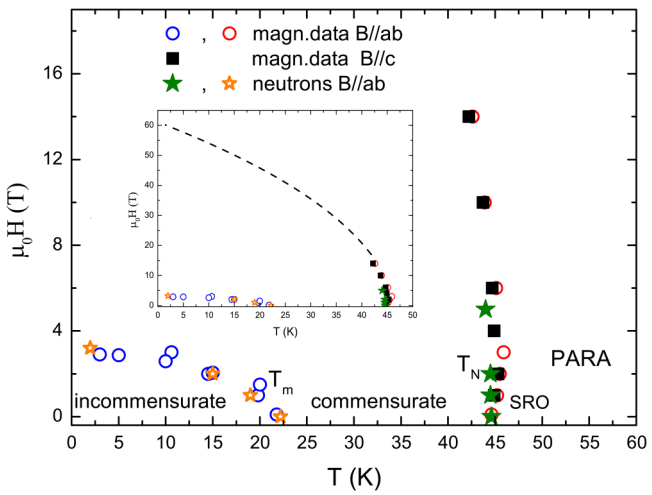

FIG. 11. Magnetic phase diagram of $NiBr_2$ constructed from magnetic bulk measurements (circles and squares) and neutron diffraction data (stars). In the inset, a crude estimate of the critical field associated with the T_N is represented.

within the basal plane in a incommensurate manner, making an angle ($\alpha \sim 9.5°$) between the two Ni moments as one moves along the *a*-axis within the plane [see Fig. 9(c)]. The relative population of magnetic domains is about 31%, 28%, and 41%.

Figure 10(a) shows the temperature dependence of the intensity measured around (0 0 3/2) position with a field of 2 T applied within the (*a*–*b*) plane. As the applied field increases above the critical value, magnetic reflections indexable with $q_c = (0\ 0\ 3/2)$ appear. Figure 10(b) depicts the temperature dependence of the intensity around (0 0 3/2) position at a field of 5 T applied within the (*a*–*b*) plane. The magnetic field enforces the retention of the commensurate phase at higher temperature.

C. Phase diagram

The magnetic phase diagram of $NiBr_2$ near critical temperature $T_m(T_N)$ has been drawn using the bulk magnetization, susceptibility, and neutron diffraction data. Below T_N, a substantial intensity inflation of the magnetic satellites results. As shown in Fig. 11, a commensurate magnetic structure exists between 45 K and 22 K with Ni moments lying in the (*a*–*b*) plane. Below 22 K at moderate magnetic fields applied along the (*a*–*b*) plane, an incommensurate magnetic structure emerges with Ni moments confined within the basal plane, rotating by an angle ($\alpha \sim 9.6°$) upon moving along the a-axis. The inset to Fig. 11 shows the extended field range, which suggests yet another field-induced transition around 60 T.

The behavior of $\chi(H, T)$ may be a defining characteristic of such transitions, mainly reflecting the unusual combination of ferromagnetic and antiferromagnetic interactions in the $NiBr_2$ system, which leads to the complicated influence of applied fields on the spin configurations along the commensurate-incommensurate boundary. According to Rastelli *et al.*,[14] when both J_{nn} and J_{nnn} are positive, the system behaves as ferromagnetic, but, when either or both are negative, helical or antiferromagnetic states are realized. A delicate balance of various exchange interactions prevails in a helical magnetic structure at lower temperatures, which enforces the system across the boundary from incommensurate-to-commensurate phase at elevated temperatures. The interplay between competing interactions leads to amplitude-modulated magnetic structure possesses a periodicity that is different from spatial distributions of spacing in the crystal.[32–35]

D. Summary and conclusions

The magnetic measurements and neutron diffraction of $NiBr_2$ single crystal reveal a systematic variation of exchange interactions and helical wave vector as a function of the applied magnetic field. The changes noticed in the magnetic properties are dominated by the variation of magnetic anisotropies and exchange interactions. A magnetic field-induced spin reorientation occurs, which entirely transforms the low-temperature incommensurate phase into a high-temperature commensurate spin phase. This behavior of the incommensurate phase is purely governed by spin-flop transition. On the methodological side, we extract definitive microscopic information about the spin triangular system of $NiBr_2$. These findings accelerate the search for exotic quantum states in helimagnetic systems through the screening of many related materials having vast scientific and novel technological implications.

ACKNOWLEDGMENTS

The authors would like to thank M. Reehuis, F. Yokoachiya, and U. Keiderling for technical help with the neutron data collection. The authors would also like to acknowledge support from CIFC, IIT (BHU) during the measurements. S.K.M. acknowledges the funding from the Indian Institute of Technology (BHU), Varanasi, India with Grant No. IIT(BHU)/R&D/SM/2016-17/4453. The authors thank Professor J. Kumar for critical reading of the manuscript.

REFERENCES

[1] A. Fert, V. Cros, and J. Sampiao, Nat. Nanotechnol. **8**, 152–156 (2013).
[2] J. Sampaio, V. Cros, S. Rohart, A. Thiaville, and A. Fert, Nat. Nanotechnol. **8**, 839–844 (2013).
[3] S. Emori, U. Bauer, S.-M. Ahn, E. Martinez, and G. S. D. Beach, Nat. Mater. **12**, 611–616 (2013).
[4] T. Kimura, J. C. Lashley, and A. P. Ramirez, Phys. Rev. B **73**, 220401(R) (2006).
[5] S. Seki, N. Kida, S. Kumakura, R. Shimano, and Y. Tokura, Phys. Rev. Lett. **105**, 097207 (2010).
[6] S. Mühlbauer, B. Binz, F. Jonietz, C. Pfleiderer, A. Rosch, A Neubauer, R. Georgii, and P. Boni, Science **323**, 915–919 (2009).
[7] U. K. Rossler, A. N. Bogdanov, and C. Pfleiderer, Nat. Lett. **442**, 797–801 (2006).
[8] I. Dzyaloshinskii, J. Phys. Chem. Solids **4**, 241–255 (1958).
[9] T. Moriya, Phys. Rev. Lett. **4**, 228 (1960).
[10] M. Azhar and M. Mostovoy, Phys. Rev. Lett. **118**, 027203 (2017).
[11] T. Masuda, A. Zheludev, A. Bush, M. Markina, and A. Vasiliev, Phys. Rev. Lett. **92**, 177201 (2004).
[12] R. Zinke, J. Richter, and S.-L. Drechsler, J. Phys. Condens. Matter **22**, 446002 (2010).
[13] J. Villain, Physica B+C, **86–88B**, 631–633 (1977).
[14] E. Rastelli, A. Tassi, and L. Reatto, Physica B+C, **97**, 1–24 (1979).

[15]F. Ye, J. A. Fernandez-Baca, R. S. Fishman, Y. Ren, H. J. Kang, Y. Qiu, and T. Kimura, Phys. Rev. Lett. **99**, 157201 (2007).
[16]J. T. Haraldsen, M. Swanson, G. Alvarez, and R. S. Fishman, Phys. Rev. Lett. **102**, 237204 (2009).
[17]R. S. Fishman and S. Okamoto, Phys. Rev. B **81**, 020402(R) (2010).
[18]R. J. Pollard, V. H. McCann, and J. B. Ward, J. Phys. C **15**, 6807 (1982).
[19]Y. Tokunaga, D. Okuyama, T. Kurumaji, T. Arima, H. Nakao, Y. Murakami, Y. Taguchi, and Y. Tokura, Phys. Rev. B **84**, 060406(R) (2011).
[20]T. Kurumaji, S. Seki, S. Ishiwata, H. Murakawa, Y. Tokunaga, Y. Kaneko, and Y. Tokura, Phys. Rev. Lett. **106**, 167206 (2011).
[21]E. N. Sickafus and D. R. Winder, J. Appl. Phys. **35**, 2541 (1964).
[22]P. Day, A. Dinsdale, E. R. Krausz, and D. J. Robbins, J. Phys. C **9**, 2481 (1976); P. Day, and K. R. A. Ziebeck, J. Phys. C **13**, L523 (1980).
[23]A. Adam, D. Billerey, C. Terrier, R. Mainard, L. P. Regnault, J. Rossat-Mignod, and P. Meriel, Solid State Commun. **35**, 1–5 (1980).
[24]L. P. Regnault, J. Rossat-Mignod, A. Adam, D. Billerey, and C. Terrier, J. Phys. France **43**, 1283–1290 (1982).
[25]T. Okubo, S. Chung, and H. Kawamura, Phys. Rev. Lett. **108**, 017206 (2012).
[26]K. Prokeš and F. Yokoachiya, J. Large-Scale Res. Facilities **3**, A104 (2017).
[27]T. Roisnel and J. Rodrguez-Carvajal, Mater. Sci. Forum **378–381**, 118–123 (2001).
[28]V. F. Sears, in *International Tables of Crystallography*, edited by A. J. C. Wilson (Kluwer, Dordrecht, 1992), Vol. C, p. 383.
[29]C. Stock, S. Jonas, C. Broholm, S. Nakatsuji, Y. Nambu, K. Onuma, Y. Maeno, and J.-H. Chung, Phys. Rev. Lett. **105**, 037402 (2010).
[30]D. I. Svergun and L. A. Feigin, in *Structure Analysis by Small-Angle X-ray and NeutronScattering*, edited by G. W. Taylor (Plenum Press, New York, 1987).
[31]A. S. Cameron, Y. V. Tymoshenko, P. Y. Portnichenko, J. Gavilano, V. Tsurkan, V. Felea, A. Loidl, S. Zherlitsyn, J. Wosnitza, and D. S. Inosov, J. Phys. Condens. Matter **28**, 146001 (2016).
[32]R. J. Birgeneau, J. Skalyo, and G. Shirane, J. Appl. Phys. **41**, 1303 (2003).
[33]N. Terada, S. Mitsuda, T. Fujii, K. Soejima, I. Doi, H. A. Katori, and Y. Noda, J. Phys. Soc. Jpn. **74**, 2604–2611 (2005).
[34]F. Heidrich-Meisner, A. Honecker, and T. Vekua, Phys. Rev. B **74**, 020403(R) (2006).
[35]R. S. Fishman, Phys. Rev. Lett. **106**, 037206 (2011).